fire

MDPI

Article

In Situ Synthesis of SiO_2/Polyimide Aerogels with Improved Thermal Safety via Introducing Methyltrimethoxysilane

Zhi Li [1], Fang Zhou [1], Kai Shen [1], Miao Liu [1], Yumin Duan [1], Jiahui Chen [1], Shuai Li [1,*] and Haoxuan Yu [2]

[1] School of Resources and Safety Engineering, Central South University, Changsha 410083, China; lizhi89@csu.edu.cn (Z.L.)
[2] School of Engineering, Monash University Malaysia, Bandar Sunway, Subang Jaya 47500, Malaysia
* Correspondence: shuaige@csu.edu.cn

Abstract

Polyimide aerogels (PIAs) possess enormous application potential in high-temperature thermal insulation scenarios. As high-efficiency thermal insulation materials, their thermal safety and thermal insulation performance are of crucial importance. Currently, poor dimensional stability, high-temperature pyrolysis, and severe shrinkage remain the key factors restricting their development and practical application. In this work, we employ an in situ co-gelation synthesis strategy, where methyltrimethoxysilane (MTMS) is introduced as the silica precursor to fabricate SiO_2/polyimide aerogels (Si@PIAs). This strategy enhances the interfacial bonding strength between the organic and inorganic phases, enabling their complementation of strengths. Experimental results demonstrate that the incorporation of the inorganic SiO_2 phase endows Si@PIAs with higher thermal safety, superior thermal insulation performance, lower density, and reduced shrinkage. Among them, Si_{10}@PIA performs best with a density of 85 mg/cm^3, a thermal conductivity of 23.28 mW/(m·K), and a heat flow peak temperature of 720.7 °C. More importantly, pyrolysis analysis reveals that the pyrolysis process of Si@PIAs shifts to a randomized nucleation and growth model ($n = 2/5$) with the mechanism function $g(\alpha) = [-\ln(1-\alpha)]^{5/2}$. Compared with pure PIAs, Si@PIAs possess stronger resistance to pyrolysis, lower gross calorific value, and improved thermal safety. This study provides theoretical and practical guidance for the development of high-performance aerogel materials, promoting their application in lithium-ion battery separators, high-temperature insulation, and fire-resistant materials.

Keywords: polyimide aerogel; SiO_2; thermal safety; pyrolysis dynamic; kinetics analysis

Check for updates

Academic Editor: Yanming Ding

Received: 19 December 2025
Revised: 31 January 2026
Accepted: 7 February 2026
Published: 12 February 2026

Copyright: © 2026 by the authors. Licensee MDPI, Basel, Switzerland. This article is an open access article distributed under the terms and conditions of the Creative Commons Attribution (CC BY) license.

1. Introduction

Polyimide aerogels (PIAs), characterized by their nanoporous architecture, combine the outstanding properties of polyimides, including high mechanical strength, superior thermal stability, and versatile synthesis routes, with the distinctive attributes of aerogels, featuring high specific surface area, high porosity, low density and low thermal conductivity [1–3]. With densities significantly lower than conventional polyimide materials ($\leq$100 mg/cm^3) and thermal conductivities ranging from 25 mW/(m·K) to 30 mW/(m·K), PIAs exhibit broad application prospects in thermal insulation [4], aerospace [5], sensor technology [6], adsorption separation [7], and electronic information [8].

Compared with typical polymer aerogels, PIAs demonstrate exceptional high-temperature stability, with an initial thermal decomposition temperature often exceeding 500 °C [9], laying a solid foundation for high-temperature applications. However,

PIAs face critical challenges, including poor dimensional stability during fabrication, high-temperature pyrolysis, and severe shrinkage under high-temperature conditions, which impede their widespread adoption [10]. Minimizing or preventing structural shrinkage and collapse of PIAs during synthesis and operation is crucial. Consequently, developing novel, high-performance composite aerogels through the hybridization of polyimides with inorganic materials featuring high thermal stability has emerged as a prominent research focus.

Silica aerogels, the most extensively studied and technologically mature aerogel materials, possess remarkable properties, such as ultra-low thermal conductivity (17–21 mW/(m·K)), low density (10–150 mg/cm^3), high porosity (>90%), and large specific surface area (500–1200 m^2/g) [11–14], enabling their application across diverse fields [15–18]. Introducing SiO_2 aerogel into polyimide matrices can preserve the inherent advantages of PIAs while mitigating thermal shrinkage issues. However, the extent to which these improvements can be achieved strongly depends on the dispersion state, interfacial compatibility, and structural continuity of the inorganic phase.

At present, numerous studies have focused on incorporating SiO_2 aerogel particles into PIAs via physical doping. For instance, Ma et al. [19] fabricated PI/SiO_2 composite aerogels, which reduced the thermal conductivity to as low as 36 mW/(m·K) while simultaneously enhancing the specific surface area and porosity. Zhang et al. [20] employed aminated SiO_2 nanoparticles as cross-linkers to prepare PI aerogels, achieving a low density of 85 mg/cm^3 and a thermal conductivity of 20.1 mW/(m·K) without compromising mechanical performance. Kantor et al. [21] embedded micrometric SiO_2 aerogel particles into the polyimide (PI) network, yielding composite materials with a thermal conductivity of merely 17.5 mW/(m·K), a dielectric constant of 1.2, and significantly improved high-temperature dimensional stability. Despite these encouraging results, most physically doped systems suffer from limited inorganic loading efficiency and weak interfacial bonding between the polymer matrix and silica particles. Particle agglomeration and heterogeneous dispersion are frequently observed, leading to local stress concentration, pore structure disruption, and a trade-off between thermal insulation performance and mechanical or thermal stability. These limitations ultimately pose a bottleneck to further property optimization.

In contrast, introducing silicon precursors to form a SiO_2 aerogel network within the polyimide matrix via the condensation of $Si(OH)_4$, thereby achieving a two-phase co-gelation, can better enhance the compatibility between the two phases and more effectively realize the complementary advantages of the two phases. Hybrid aerogels based on interpenetrating sol–gel networks formed via co-gelation of organic and inorganic phases have been reported in previous studies, demonstrating the feasibility of this strategy. For example, Rhine et al. [22] systematically proposed and realized the formation of interpenetrating networks of metal oxide and polyimide gels through sol–gel processing. In addition, Leventis et al. [23] showed that the synthesis of metal oxide/organic interpenetrating networks is both simple and highly versatile, and can essentially be achieved by straightforward mixing of two precursor solutions. At the same time, silica/polyimide aerogels have also been prepared by other researchers using co-gelation approaches. Xiao et al. [24] prepared silica/polyimide aerogels with both superhydrophobicity and elasticity based on a dual-constraint growth strategy in a co-sol system. However, freeze-drying still leads to pore structure defects and agglomeration of the inorganic silicon phase, making it difficult to optimize their thermal insulation performance and thermal safety performance. Yan et al. [25] and Zhu et al. [26] separately employed methyltrimethoxysilane (MTMS) as the silicon precursor for co-gelation with polyimide, focusing on the acoustic properties and radar stealth performance of the resulting composites, respectively. Notably, a systematic

investigation of how in situ-generated SiO_2 aerogels influence the thermal stability, pyrolysis behavior, and thermal safety of polyimide aerogels remains lacking. In particular, the underlying mechanisms governing the evolution of pyrolysis kinetics and decomposition pathways after inorganic phase incorporation have not yet been fully elucidated. These unresolved issues form the main focus and scientific motivation of the present study.

Therefore, in this study, we prepared SiO_2/polyimide aerogel (Si@PIA) composites by introducing MTMS through in situ co-gelation, aiming to harness the complementary advantages of organic and inorganic phases and thereby modulate the thermal insulation performance and thermal safety of Si@PIA composites. Systematic experiments were performed to investigate the effects of inorganic SiO_2 aerogel incorporation on the basic physicochemical properties, microstructure, and thermal behavior of Si@PIA composites. Particular emphasis was placed on the thermal safety characteristics of the composites, including thermal stability, pyrolysis kinetics, pyrolysis mechanism models, and gross calorific value. These investigations are intended to provide novel insights into the regulation of thermal safety performance for polyimide-based aerogels.

2. Materials and Methods

2.1. Raw Materials

3,3′,4,4′-Biphenyltetracarboxylic dianhydride (BPDA, 97%, Aladdin, Shanghai, China), 4,4′-Diaminodiphenyl ether (ODA, 98%, Aladdin, Shanghai, China) were used as the dianhydride and diamine monomers, respectively, to construct the polyimide backbone via the poly (amic acid) (PAA) precursor route. Bis [3-(trimethoxysilyl)propyl] amine (BTMSPA, 90%, Aladdin, Shanghai, China) was employed as an organosilane coupling agent, and Methyltrimethoxysilane (MTMS, 98%, Aladdin, Shanghai, China) served as the primary silica precursor for the in situ formation of the SiO_2 network. Cetyltrimethylammonium bromide (CTAB, 99%, Aladdin, Shanghai, China) was introduced as surfactant. Nitric acid (HNO_3, 36–38%, Aladdin, Shanghai, China) and Ammonia water ($NH_3 \cdot H_2O$, 25–28%, Sinopharm, Shanghai, China) were utilized as acid-base catalysts to facilitate the hydrolysis and polycondensation reactions of MTMS. Pyridine (99.5%, Aladdin, Shanghai, China) and propionic anhydride (99%, Titan, Shanghai, China) were used as reagents for chemical imidization, while N-methyl-2-pyrrolidinone (NMP, 99%, Titan, Shanghai, China) served as a polar aprotic solvent during the synthesis and co-gelation process. Ethanol (EtOH, 99.7%, Sinopharm, Shanghai, China) was used as the solvent for solvent exchange to remove residual solvents and unreacted impurities. Purified water was prepared in the laboratory with an ultrapure water system (ECO-S, HHitech, Shanghai, China).

2.2. Preparation of Si@PIAs

The preparation of polyimide aerogels was accomplished via the DuPont two-step method, with chemical imidization selected as the imidization technique. To achieve the co-gelation of organic and inorganic phases, MTMS was in situ incorporated as the silica precursor. Firstly, a certain amount of MTMS, 0.1 g of CTAB, and 5.5 mL of NMP were mixed and stirred. Subsequently, 6 mL of 0.1 M HNO_3 was added, and the mixture was stirred at room temperature under ambient pressure for 40 min to form silicon sol A. Secondly, 0.7814 g of ODA (3.902 mmol) was dissolved in 15.568 mL of NMP, followed by the slow, stepwise addition of 1.1769 g of BPDA (4 mmol). The reaction between ODA and BPDA yielded a PAA solution. Next, 215 μL of BTMSPA was added to the PAA solution and stirred for 10 min to induce cross-linking, forming solution B.

Thirdly, 2 mL of solution A (silicon sol) was slowly added to solution B and stirred for 15 min to ensure thorough mixing of the inorganic silicon phase and the polyimide organic phase, thereby promoting the organic–inorganic interaction. Subsequently, 230 μL

of concentrated $NH_3 \cdot H_2O$ (26.5%) was added and stirred for 3 min to facilitate the polycondensation of Si-O-Si bonds. During the gelation stage, 4.103 mL of propionic anhydride and 2.575 mL of pyridine were added and stirred for 3–5 min to promote the imidization reaction. The resulting mixture was cast into molds and allowed to gel for 12–24 h to strengthen the gel network and structure.

After demolding, the hybrid gel were subjected to solvent exchange with ethanol for 48 h in a water bath at 55 °C to remove residual solvents and unreacted impurities. Notably, during this process, the ethanol was replaced every 12 h to ensure a more complete solvent exchange. Finally, the gels were dried under supercritical conditions at 60 °C and 11 MPa for 48 h. After a pressure release process lasting 24–48 h, the final samples were obtained. The detailed preparation process is illustrated in Figure 1.

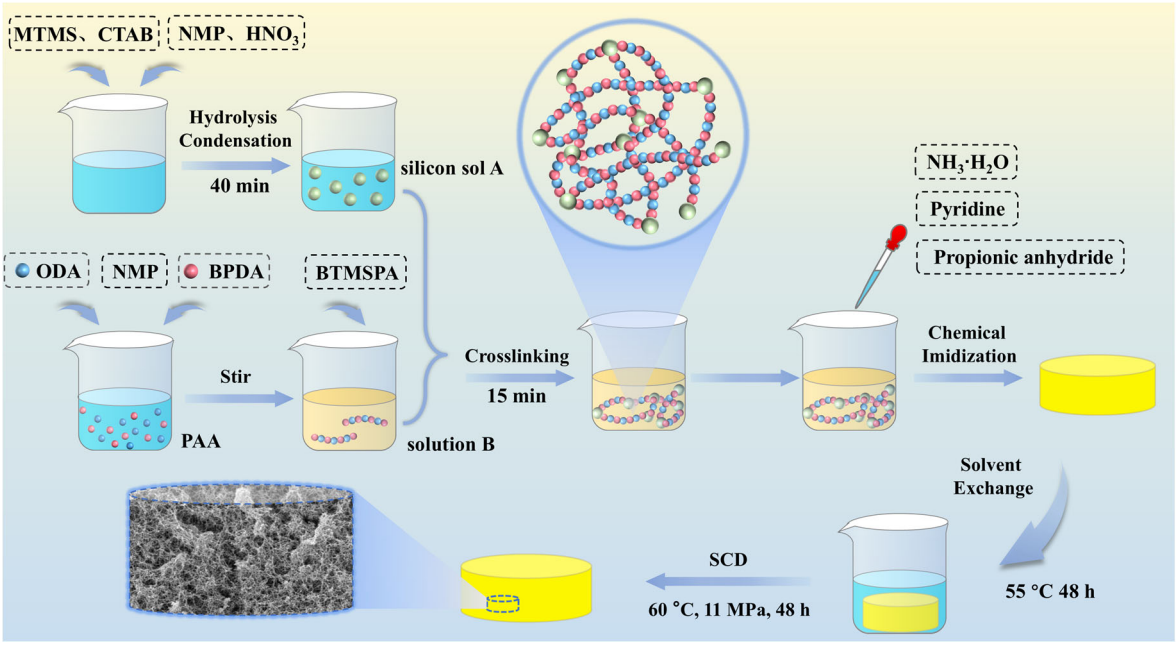

Figure 1. Schematic illustration of the process for synthesizing SiO_2/polyimide aerogel (Si@PIA) composites.

To minimize the impact of the volume of silica sol A on the construction of the polyimide aerogel network, its introduction amount was fixed at 2 mL. The content of the MTMS silica source in silica sol A was varied to increase the amount of inorganic silica phase introduced. For ease of presentation, the aerogel composites prepared from silica sols with different MTMS contents were named Si_x@PIA, where x represents the volume of MTMS in the silica sol. For example, the content of the MTMS silica source in the silica sol was 5 mL, and the finally prepared aerogel composite was Si_5@PIA. In this chapter, Si_5@PIA, Si_{10}@PIA, Si_{15}@PIA, and Si_{20}@PIA were prepared. For each composition, at least 3 independently prepared samples were used for characterization and data analysis to ensure reproducibility.

2.3. Characterization of Physicochemical Properties

The apparent density (ρ_b) of polyimide aerogel composites was calculated by the ratio of mass to volume. The mass of cylindrical samples was measured using an electronic balance, and the volume was obtained by measuring the bottom diameter and height of the samples with a vernier caliper and calculating according to the volume formula for a cylinder.

During the gelation and supercritical drying stages of the preparation process, close packing between polyimide molecular chains tends to occur, leading to significant linear (volumetric) shrinkage. To characterize the structural strength and stability of the polyimide aerogel gel network, the radial shrinkage rate during Si@PIAs preparation was calculated using the following formula:

$$S_R = \frac{D_0 - D}{D_0} \times 100\% \quad (1)$$

where D_0 is the gel diameter after casting into a mold (identical to the mold diameter, 50 mm), and D is the diameter of the final sample after supercritical drying.

For microscopic structural and surface morphology analysis, field-emission scanning electron microscopy (SEM, Sigma 300, Carl Zeiss AG, Jena, Germany) was employed. Small aerogel fragments were attached to conductive tape on a sample stage and sputter-coated with gold for 150 s using a mini ion sputter coater (Mini Coater, Supro Co., Ltd., Shenzhen, China) to improve conductivity and imaging resolution.

N_2 adsorption–desorption tests were conducted at 77 K using an automatic specific surface area and porosity analyzer (ASAP 2460, Micromeritics Instrument Corp., Norcross, GA, USA). Samples were degassed at 120 °C for 12 h to obtain adsorption–desorption isotherms, allowing characterization of the three-dimensional nanoporous structure and pore parameters. Specific surface area was calculated via the Brunauer–Emmett–Teller (BET) method, while pore size distribution and porosity parameters were determined using the Barrett–Joyner–Halenda (BJH) method under the assumption of cylindrical pores. It should be noted that nitrogen adsorption–desorption analysis has inherent limitations in fully describing larger mesopores and macropores, particularly for highly open porous materials [27]. In addition, due to the highly porous and mechanically fragile nature of silica aerogels, structural deformation of the skeleton may occur during the nitrogen sorption process [28], which can affect the accuracy of the measurement results. Therefore, nitrogen sorption results in this study are mainly used to characterize mesoporous features and relative changes in pore structure, while larger mesopores and macropores can be observed via SEM.

Fourier transform infrared spectroscopy (FTIR, Nicolet iS50, Thermo Fisher lnc., Waltham, MA, USA) was used to identify the chemical reactions, distinct functional groups and chemical bonds in Si@PIAs. Samples were dried prior to testing to remove residual moisture, and attenuated total reflection (ATR) mode was applied with a spectral range of 4000–400 cm^{-1}.

Thermal conductivity was measured using a transient hot-wire method with a thermal conductivity analyzer (T3000E, XIATECH Instrument Co., Ltd., Xi'an, China). To minimize air disturbance, two identical parallel samples were placed in a custom acrylic chamber and tested at room temperature. A 100 g weight was applied to the upper sample to ensure close contact between the samples and the central test probe.

Thermal stability of Si@PIAs was evaluated via thermogravimetric-differential scanning calorimetry (TG-DSC) using a simultaneous thermal analyzer (STA 8000, PerkinElmer Inc., Waltham, MA, USA). Tests were performed under air atmosphere with a heating rate of 10 K/min over the range of 30–900 °C.

Thermogravimetric analysis (TGA) of polyimide aerogel samples was performed using a simultaneous thermal analyzer (STA 449 F3, NETZSCH-Gerätebau GmbH, Selb, Germany) under air and nitrogen atmospheres, with the temperature ramp ranging from 30 °C to 900 °C. The heating rates (β) were set at 5 K/min, 10 K/min, and 20 K/min, which are the most commonly used rates for studying the slow pyrolysis of solid materials in this field [29]. Based on the thermogravimetric data at different heating rates, the thermo-oxidative/pyrolytic processes of Si@PIAs were analyzed, and kinetic/thermodynamic

parameters were calculated. This study comparatively analyzed the thermo-oxidative and pyrolytic processes of Si@PIAs using model-free methods and determined corresponding apparent activation energies, entropy changes, enthalpy changes, and other kinetic/thermodynamic parameters. Additionally, Si@PIAs samples were subjected to drying under 150 °C for 1 h before TGA testing to rule out the effects of residual moisture and organic solvents.

The thermo-oxidative process of materials is crucial for thermal safety analysis in most practical application scenarios, while the pyrolytic process avoids interference from oxidation reactions and focuses more on the intrinsic thermal safety characteristics of the material itself. Therefore, based on a clear understanding of their thermo-oxidative/pyrolytic processes, the pyrolytic mechanism of Si@PIAs was further analyzed, and the most probable pyrolytic reaction mechanism model was confirmed via model-fitting methods.

An oxygen bomb calorimeter (AM-C1009, Changsha Yuanfa Instrument Co., Ltd., Changsha, China) was utilized for the determination of the gross calorific value (GCV) of Si@PIAs.

2.4. Pyrolysis Kinetics and Thermodynamics

2.4.1. Model-Free Method

After analyzing and fitting thermogravimetric data obtained at different heating rates (β), model-free methods, such as the Flynn-Wall-Ozawa (FWO) and Kissinger-Akahira-Sunose (KAS) methods were used to calculate the apparent activation energy changes during the pyrolysis processes of Si@PIAs. These approaches were recognized as more reliable for non-isothermal kinetic analysis due to their independence from specific reaction models and ability to determine apparent activation energies as a function of conversion across different heating rates [30,31].

Other kinetic/thermodynamic parameters such as pre-exponential factors, entropy changes (ΔS), and enthalpy changes (ΔH) were also calculated. To avoid the influence of oxygen in the air and specifically analyze the intrinsic thermal safety characteristics of Si@PIAs, model-fitting methods such as the Coats–Redfern (CR) method and Malek's method were used to deeply analyze the pyrolysis process of Si@PIAs in an inert atmosphere and identify its most probable pyrolysis mechanism function. The expression for the KAS method is presented as follows [32],

$$\ln\left(\frac{\beta}{T^2}\right) = \ln\left(\frac{AR}{Eg(\alpha)}\right) - \frac{E}{RT} \tag{2}$$

where β is the heating rate, A is the pre-exponential factor, R is the ideal gas constant (8.314 J/K/mol), α is the conversion rate, and E is the apparent activation energy. The value of the E can be calculated from the slope of the fitting curve with the abscissa of $1/T$ and the ordinate of $\ln(\beta/T^2)$. The FWO method is expressed as follows [33,34],

$$\ln\beta = \ln\left(\frac{AE}{Rg(\alpha)}\right) - 5.3308 - 1.0516\frac{E}{RT} \tag{3}$$

Here in, A, E, α, and R refer to the same parameters as in the KAS method. The activation energy can be calculated from the slope of the fitting curve with the horizontal axis of $1/T$ and the vertical axis of $\ln\beta$.

After the calculation of the E, kinetic/thermodynamic parameters such as the A, ΔH, Gibbs free energy (ΔG), and ΔS can be calculated using the following equations [35,36]. The relevant data measured at a β of 10 K/min were selected for the calculations.

$$A = \frac{\beta E}{RT_m^2} e^{\frac{E}{RT_m}} \tag{4}$$

$$\Delta H = E - RT \tag{5}$$

$$\Delta G = E + RT_m \ln\left(\frac{k_B T_m}{hA}\right) \tag{6}$$

$$\Delta S = \frac{\Delta H - \Delta G}{T_m} \tag{7}$$

in which, E represents the apparent activation energy derived via the model-free method, T_m is the peak temperature in the derivative thermogravimetric (DTG) curve, k_B is the Boltzmann constant (1.381×10^{-23} J/K), and h is the Planck constant (6.626×10^{-34} J·s).

2.4.2. Model-Fit Method

The model-fit method can be used to further solve the most general reaction mechanism function of the pyrolysis process and then elucidate its pyrolysis process. Among them, the CR method is a more common method, which can be used to further predict the reaction mechanism model of the pyrolysis process, and give the corresponding mechanism function [37]:

$$\ln\left(\frac{g(\alpha)}{T^2}\right) = \ln\left(\frac{AR}{\beta E}\right) - \frac{E}{RT} \tag{8}$$

Using common reaction models, such as chemical reaction models, diffusion models, shrinkage models, and random nucleation growth models [29,38], the activation energy E can be derived from the slope obtained by linear least squares fitting of $\ln(g(\alpha)/T^2) \sim 1/T$. Common reaction models and their mechanistic functions are listed in Table 1.

Table 1. Common reaction models and mechanism functions for pyrolysis of solid.

Reaction Model			$f(\alpha)$	$g(\alpha)$
Chemical reaction	Zero-order	F0	1	α
	First-order	F1	$(1-\alpha)^1$	$-\ln(1-\alpha)$
	Second-order	F2	$(1-\alpha)^2$	$(1-\alpha)^{-1}-1$
	Third-order	F3	$(1-\alpha)^3$	$[(1-\alpha)^{-2}-1]/2$
	Multi-order	Fn	$(1-\alpha)^n$	$[(1-\alpha)^{1-n}-1]/(n-1)$
Diffusion control reaction	One-dimensional diffusion	1-D	$1/2\alpha$	α^2
	Two-dimensional diffusion	2-D	$1/[-\ln(1-\alpha)]$	$(1-\alpha)\ln(1-\alpha)+\alpha$
	Three-dimensional diffusion (Jander)	3-D (J)	$1.5(1-\alpha)^{2/3}/[1-(1-\alpha)^{1/3}]$	$[1-(1-\alpha)^{1/3}]^2$
	Three-dimensional diffusion (Ginstling-Brounshtein)	3-D (GB)	$3/[2((1-\alpha)^{-1/3}-1)]$	$1-2\alpha/3-(1-\alpha)^{2/3}$
	Three-dimensional diffusion (Zhuravlev)	3-D (ZH)	$1.5(1-\alpha)^{4/3}[(1-\alpha)^{-1/3}-1]^{-1}$	$[(1-\alpha)^{-1/3}-1]^2$
Phase boundary reaction	Contracting cylinder (cylindrical symmetry)	R2	$2(1-\alpha)^{1/2}$	$1-(1-\alpha)^{1/2}$
	Contracting sphere (spherical symmetry)	R3	$3(1-\alpha)^{2/3}$	$1-(1-\alpha)^{1/3}$
Nucleation and growth reaction	Avrami–Erofeyev (n = 2/5)	$A_{2/5}$	$(2/5)(1-\alpha)[-\ln(1-\alpha)]^{-3/2}$	$[-\ln(1-\alpha)]^{5/2}$
	Avrami–Erofeyev (n = 1/2)	$A_{1/2}$	$1/2(1-\alpha)[-\ln(1-\alpha)]^{-1}$	$[-\ln(1-\alpha)]^2$
	Avrami–Erofeyev (n = 2)	A_2	$2(1-\alpha)[-\ln(1-\alpha)]^{1/2}$	$[-\ln(1-\alpha)]^{1/2}$
	Avrami–Erofeyev (n = 3)	A_3	$3(1-\alpha)[-\ln(1-\alpha)]^{2/3}$	$[-\ln(1-\alpha)]^{1/3}$
	Avrami–Erofeyev (n = x)	A_n	$n(1-\alpha)[-\ln(1-\alpha)]^{1-1/n}$	$[-\ln(1-\alpha)]^{1/n}$

The Malek method is a fitting approach for selecting kinetic models through $y(\alpha)$ curves, which involves comparing the theoretical curves of different kinetic reaction mech-

anisms with actual experimental curves. The mechanism model with the highest degree of coincidence is considered as the mechanism for the pyrolysis reaction process, thereby determining the most probable reaction mechanism function $g(\alpha)$.

The theoretical curves of different pyrolysis models also use α as the abscissa and $y(\alpha)$ as the ordinate, with the specific calculation formula shown in Equation (9):

$$y(\alpha) = \frac{f(\alpha) \cdot g(\alpha)}{f(0.5) \cdot g(0.5)} \tag{9}$$

The experimental curve also takes α as the horizontal axis and $y(\alpha)$ as the vertical axis, and the specific calculation formula is shown in Equation (10):

$$y(\alpha) = \left(\frac{T_i}{T_{0.5}}\right)^2 \cdot \frac{\left(\frac{d\alpha}{dt}\right)_i}{\left(\frac{d\alpha}{dt}\right)_{0.5}} \tag{10}$$

Here, T_i and $T_{0.5}$ denote the temperatures at conversion rates $\alpha = i$ and $\alpha = 0.5$, respectively. $(d\alpha/dt)_i$ and $(d\alpha/dt)_{0.5}$ represent the reaction rates at these two conversion degrees.

Furthermore, a novel comprehensive model deviation is defined as the numerical average of the model deviations from the CR and Malek methods for each reaction model, as shown in Equation (11) [39].

$$\varepsilon = \frac{e+y}{2} = \frac{\left|\frac{E-E_0}{E_0}\right| + \left(\sum_{\alpha=1}^{n}\left|\frac{y_\alpha - y_0}{y_0}\right|\right)/n}{2} \tag{11}$$

Here, e and y correspond to the model deviations derived from the CR and Malek methods, respectively. E refers to the activation energy determined by the CR method, E_0 denotes the activation energy obtained via model-free methods (KAS and FWO methods), y_α is the theoretical value calculated by different model mechanism functions, and y_0 is the experimental value.

The reaction model exhibiting the lowest comprehensive model deviation is deemed the optimal choice. Such a comprehensive strategy contributes to elevating the accuracy of defining the most probable pyrolysis mechanism function model.

3. Results and Discussion

3.1. Thermal Stability

TG-DSC was utilized to investigate the changes in thermal stability induced by the incorporation of the inorganic SiO_2 phase. The TG-DSC curves of Si@PIAs measured under an air atmosphere are illustrated in Figure 2. The results demonstrate that the thermal decomposition occurs in three distinct stages. Below 200 °C, minor mass loss occurs due to evaporation of moisture and residual solvents, while the 270–470 °C range features mass loss from the initial thermal decomposition of polyimide, incompletely hydrolyzed MTMS and trace CTAB [40]. As the temperature rises to 500–700 °C, intense mass loss corresponds to the primary decomposition step, as evidenced by a distinct exothermic peak in the DSC curve, leaving only 0.9–2.1% residual mass. Given that water serves as the primary solvent in MTMS hydrolysate, excessive introduction tends to disrupt the gelation process of polyimide. Hence, experimental design standardized silica sol addition at 2 mL, yielding Si@PIAs with minimal inorganic silica phase content. Although this slightly delays PIA thermal degradation, the residual SiO_2 content remains negligible.

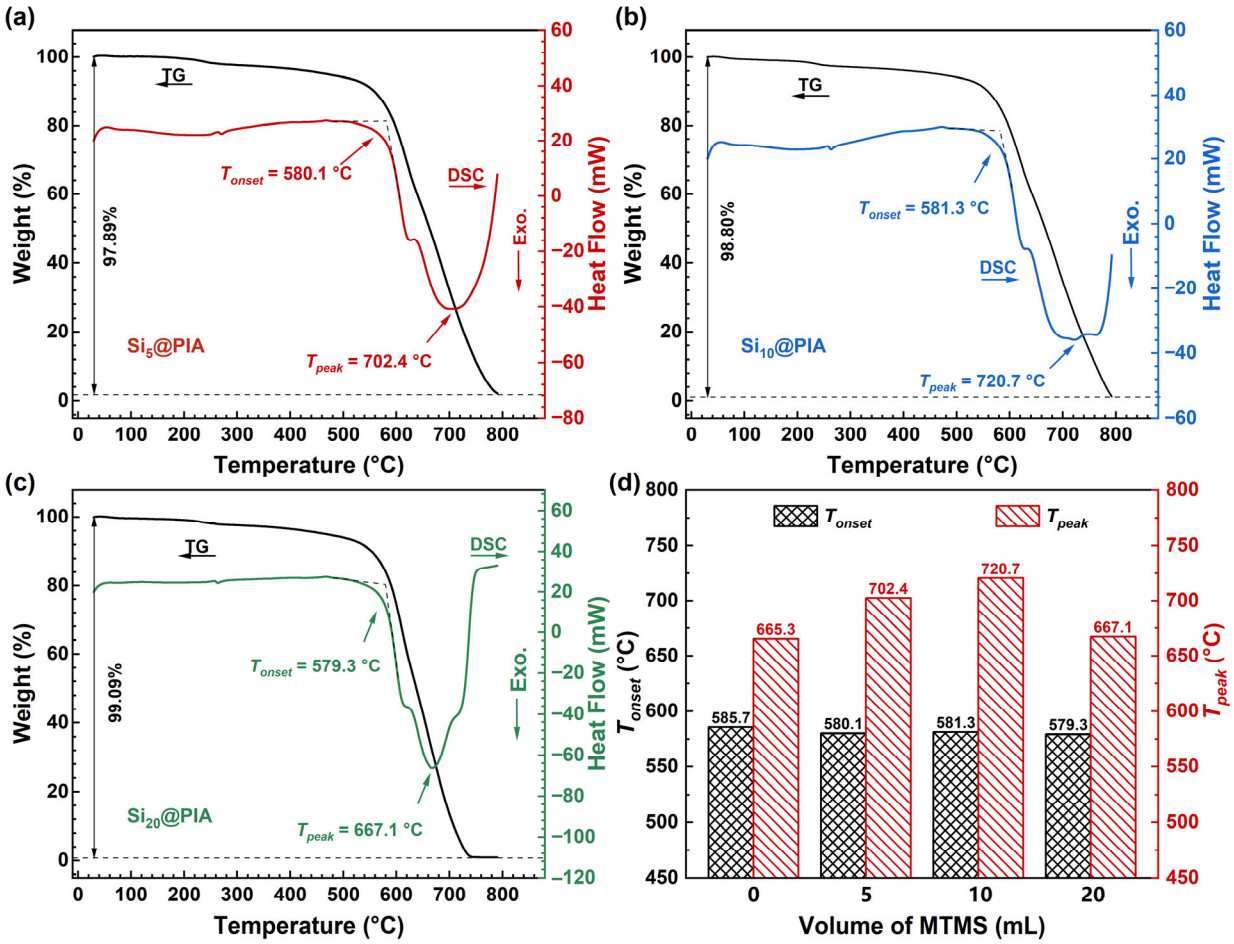

Figure 2. TG-DSC curves (**a**–**c**), the onset decomposition temperature (T_{onset}) and the peak decomposition temperature (T_{peak}) (**d**) of Si@PIAs and pure PIAs [39], the dashed lines in (**a**–**c**) indicate the extrapolated tangent used to determine T_{onset}, and the horizontal dashed line represents the residual mass after thermal decomposition.

The onset decomposition temperature (T_{onset}) and the peak decomposition temperature (T_{peak}) of the Si@PIAs can be determined from the DSC curves. A comparison of the T_{onset} and T_{peak} values for Si@PIAs with different silica loadings is presented in Figure 2d, while the corresponding data for the pure PIAs are taken from previous studies [39]. It can be observed that, compared with pure PIAs, the T_{onset} of Si@PIAs remains nearly unchanged, which is slightly different from some previously reported SiO_2/polyimide aerogel composites where a modest increase in T_{onset} was observed after introducing the inorganic silica phase [19,20,24,26]. However, it is worth noting that in most of these studies, the reported T_{onset} values remain below 560 °C, which is significantly lower than the approximately 580 °C observed in the present work. From this perspective, the Si@PIA composites developed in this study still exhibit a clear advantage in terms of onset thermal stability. Moreover, although T_{onset} remains nearly unchanged in the present system, a pronounced increase in the T_{peak} is observed with appropriate incorporation of the inorganic silica phase. These results suggest that moderate inorganic silica incorporation enhances the thermal stability of polyimide aerogels.

Specifically, the T_{peak} values of Si_5@PIA and Si_{10}@PIA reach 702.4 °C and 720.7 °C, respectively, indicating an increase of 37.1–55.4 °C compared with that of the pure polyimide aerogel (665.3 °C). This enhancement can be attributed to the moderate incorporation of the inorganic silica phase, which enables the formation of a continuous or semi-continuous silica-derived network that is relatively uniformly dispersed within the polyimide aero-

gel matrix, consistent with the subsequent SEM observations. Under high-temperature conditions, such a network effectively hinders oxygen diffusion toward the organic skeleton and retards the escape of pyrolysis volatiles, thereby delaying the thermo-oxidative degradation of polyimide and significantly enhancing the thermal stability during the main decomposition stage, as reflected by the pronounced upward shift in T_{peak}.

With a further increase in inorganic silica content, the T_{peak} of Si_{20}@PIA drops back to 667.1 °C, approaching that of the pure PIAs. In this case, excessive silica incorporation leads to enhanced local aggregation of the inorganic phase and increased structural heterogeneity, as evidenced by the subsequent SEM image. Such microstructural evolution reduces the continuity of the skeleton network and decreases the effective interfacial contact area between the organic and inorganic phases, thereby weakening the overall thermal barrier effect of the silica phase at elevated temperatures. Consequently, the pyrolysis behavior of the composite aerogel tends to approach that of the pure polyimide aerogel matrix, resulting in a T_{peak} value comparable to that of pure PIAs.

3.2. Pyrolysis Behavior and Kinetics Analysis

3.2.1. Pyrolysis Process

To elucidate the pyrolysis kinetics of Si@PIAs, TGA was performed on Si_{20}@PIA (the aerogel composites with the highest MTMS loading) under nitrogen at varying heating rates. The TG and DTG curves are shown in Figure 3a. Compared with pure PIAs [39], the residual mass of Si@PIAs increases from 63.70% to 65.25%. Additionally, the peak temperatures of the thermogravimetric curves rise from 583.2 °C to 612.9 °C as the heating rate increases from 5 to 20 K/min. This is a common feature of non-isothermal pyrolysis kinetics [41]. In addition, under non-isothermal conditions, when a temperature difference exists between the sample and the instrument temperature sensor (thermal lag), and when temperature gradients arise within the sample due to finite heat diffusion, the reaction-rate history may be distorted, thereby further amplifying this apparent temperature shift [42]. Although the kinetic parameters extracted from non-isothermal TGA data cannot be regarded as strictly intrinsic kinetic parameters when heating rate effects and thermal lag are involved, they can still be used to compare the relative pyrolysis behaviors and mechanism evolution of Si@PIAs with the pure PIAs reported in our previous work [39], given that the test conditions were kept consistent for both systems.

The pyrolysis kinetics results derived from KAS and FWO methods are shown in Figure 3b,c and Table 2. The plots of $\ln(\beta/T^2)$ versus $1/T$ and $\ln(\beta)$ versus $1/T$ at different conversion rates α exhibit good linear relationships, with determination coefficients (R^2) greater than 0.99 for all α values except α = 0.2. This validates the applicability of model-free methods for characterizing the pyrolysis behavior of Si@PIAs.

Table 2. Apparent activation energy (E) and R^2 parameters of the pyrolysis for SiO_2/polyimide aerogels (Si@PIAs) in nitrogen atmosphere based on KAS and FWO.

α	KAS		FWO		Average
	E (kJ/mol)	R^2	E (kJ/mol)	R^2	E (kJ/mol)
0.2	391.21	0.9685	385.08	0.9705	388.14
0.3	360.74	0.9948	356.42	0.9952	358.58
0.4	357.12	0.9969	353.19	0.9971	355.15
0.5	359.59	0.9994	355.74	0.9994	357.66
0.6	370.16	0.9996	365.99	0.9996	368.07
0.7	414.58	0.9997	408.48	0.9997	411.53
0.8	615.37	0.9989	599.80	0.9989	607.58
Average	409.82		403.53		406.68

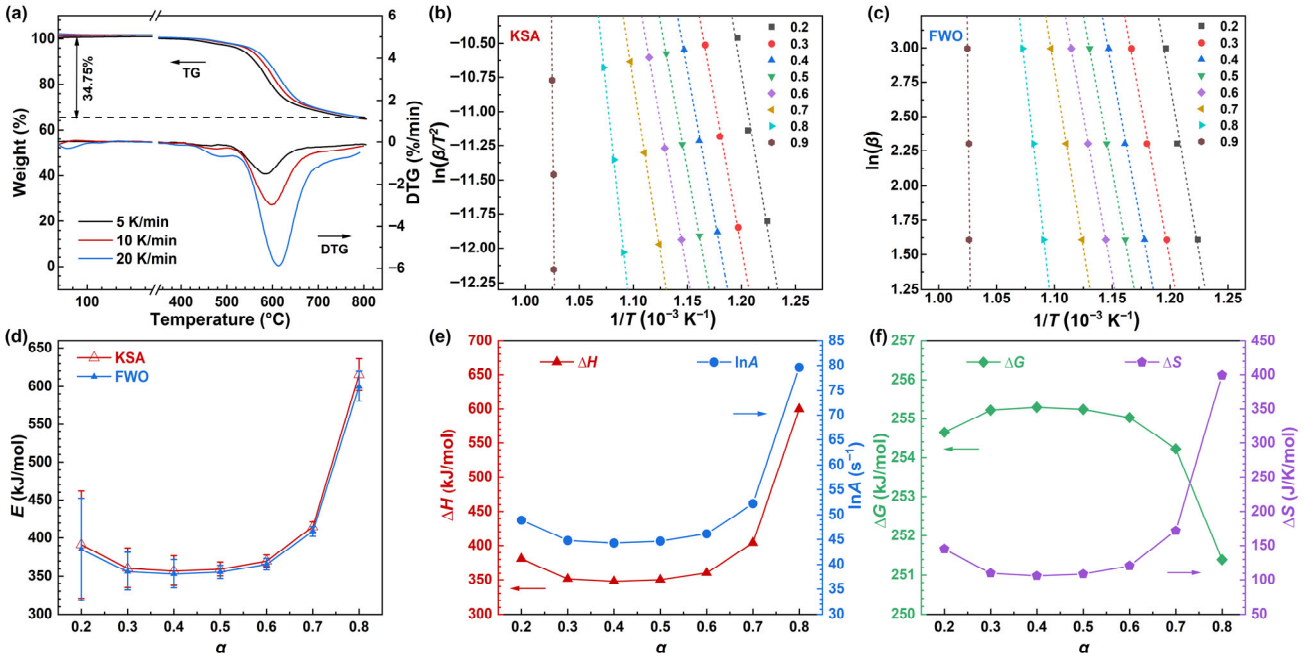

Figure 3. TG-DTG of Si_{20}@PIA (**a**), kinetic parameter fitting lines (**b**,**c**) under different heating rates during pyrolysis in a nitrogen atmosphere based on KAS and FWO methods, apparent activation energy (E) of Si_{20}@PIA (**d**) across various α and thermal dynamic parameters (**e**,**f**) in the pyrolysis process.

The E of the pyrolysis reaction was accurately calculated from the slopes of the fitted curves. Figure 3d illustrate the trend of E during the pyrolysis of Si@PIAs. Similar to pure PIAs [39], when α is below 0.7 ($T \leq 628.88$ °C), E increases gradually. As temperature rises, chemical activity decreases, requiring higher energy to drive the pyrolysis process. With further progression of pyrolysis, E sharply increases to over 600 kJ/mol.

Compared to PIAs [39], the average E of Si@PIAs during pyrolysis significantly increases from 274.61 kJ/mol to 406.68 kJ/mol, indicating that the pyrolysis of Si@PIAs is much more difficult. Under the same conditions, Si@PIAs can maintain structural integrity and performance stability for a longer time, demonstrating superior thermal safety characteristics.

Key kinetic and thermodynamic parameters of Si@PIAs pyrolysis, including ΔH, A, ΔG, and ΔS, are presented as functions of conversion rate α in Figure 3e,f, with specific data listed in Table S1. These parameters quantitatively describe the energy changes and reaction barriers during the pyrolysis, underscoring the complexity of the pyrolysis reaction. In Figure 3e, ΔH remains relatively constant for $0.2 < \alpha < 0.6$, followed by a sharp increase. This indicates that initial pyrolysis occurs under mild conditions, whereas breaking stable bonds in Si@PIAs requires higher energy input at advanced stages. The A follows the same trend as ΔH, with a significant increase in the late pyrolysis stage, reflecting enhanced molecular activity, increased effective collision frequency, and accelerated reaction kinetics as pyrolysis progresses.

As shown in Figure 3f, ΔG remains essentially stable in the early pyrolysis stage, with a value of approximately 255 kJ/mol, but decreases rapidly when $\alpha > 0.6$, indicating increased reaction spontaneity as pyrolysis progresses, while ΔS, representing system disorder, remains relatively constant initially, suggesting minimal product formation and molecular rearrangement. As pyrolysis proceeds, gaseous pyrolysis products drive a substantial increase in system disorder, enhancing randomness and elevating entropy.

3.2.2. Pyrolysis Mechanism

To address the limitation of model-free methods in determining pyrolysis mechanisms, model-fit methods were employed to quantitatively analyze the pyrolysis of Si@PIAs, clarify the differences from pure PIAs and elucidate the role of the inorganic silica phase in Si@PIAs. Calculations used the CR method, with model validation via the Malek method to identify the most probable mechanism function for Si@PIAs pyrolysis.

Figure 4a–c shows the CR method fitting curves based on heating rates of 5 K/min, 10 K/min, and 20 K/min. Following linear fitting of $\ln(g(\alpha)/T^2)$ versus $1/T$, the E was calculated from the slope. The fitting calculations for the $0.2 < \alpha < 0.7$ stage are listed in Table 3. The model-free method gave an average E of 373.19 kJ/mol for the corresponding interval in Si@PIAs. Notably, the F5 chemical reaction model (n = 5, representing a fifth-order reaction) yielded an E of 362.34 kJ/mol, which was closest to the model-free result, with an R^2 of 0.974.

Table 3. E values for Si@PIAs pyrolysis at varied heating rates derived from different reaction models through the CR method.

Reaction Model	5 K/min		10 K/min		20 K/min		Average	
	E (kJ/mol)	R^2	E (kJ/mol)	R^2	E (kJ/mol)	R^2	E (kJ/mol)	R^2
F0	91.98	0.979	96.26	0.983	92.68	0.992	93.64	0.985
F1	128.47	0.996	134.18	0.998	129.01	0.999	130.55	0.998
F2	174.25	0.999	181.73	0.998	174.48	0.994	176.82	0.997
F3	228.76	0.994	238.33	0.992	228.54	0.984	231.88	0.990
F4	290.56	0.987	302.49	0.984	289.80	0.973	294.28	0.981
F5	357.96	0.980	372.46	0.977	356.61	0.964	362.34	0.974
1-D	198.13	0.982	206.89	0.985	199.87	0.993	201.63	0.987
2-D	219.54	0.988	229.15	0.991	221.22	0.996	223.30	0.992
3-D (J)	244.72	0.994	255.32	0.995	246.28	0.998	248.77	0.996
3-D (GB)	227.89	0.990	237.82	0.993	229.53	0.997	231.74	0.993
3-D (ZH)	299.57	0.998	312.30	0.999	300.81	0.998	304.23	0.999
R2	109.07	0.990	114.03	0.992	109.71	0.997	110.94	0.993
R3	115.28	0.993	120.48	0.995	115.89	0.998	117.21	0.995
$A_{2/5}$	342.42	0.997	357.00	0.998	344.28	0.999	347.90	0.998
$A_{1/2}$	271.10	0.997	282.72	0.998	272.52	0.999	275.45	0.998
A_2	57.15	0.995	59.91	0.997	57.25	0.999	58.10	0.997
A_3	33.38	0.993	35.15	0.996	33.33	0.998	33.95	0.996

However, kinetic model selection should not rely solely on fitting deviation but must also consider the physical meaning of the model [41]. For complex solid-state decomposition processes, such as the pyrolysis of polymeric and hybrid materials, reaction orders obtained from model-fitting are generally regarded as apparent or phenomenological parameters, which describe the overall rate behavior rather than elementary reaction steps [43]. In this context, high-order reaction models, including the F5 model, are often interpreted as global kinetic descriptions rather than direct representations of the underlying reaction mechanism. Therefore, although the F5 model yields an activation energy close to that obtained by model-free methods, its physical significance in describing the pyrolysis mechanism of Si@PIAs should be interpreted with caution. The F5 model assumes a fifth-order reaction, which requires simultaneous effective collisions of five reactant molecules. Such a scenario has negligible probability in real systems, making fifth-order reactions highly implausible. Thus, the pyrolysis mechanism of Si@PIAs still requires further clarification. In contrast, the random nucleation and growth model (n = 2/5) gave a fitting result of 347.90 kJ/mol with an extremely high R^2 of 0.998. The F4 and 3-D (ZH) models also showed good agreement, necessitating further analysis and validation using the Malek method.

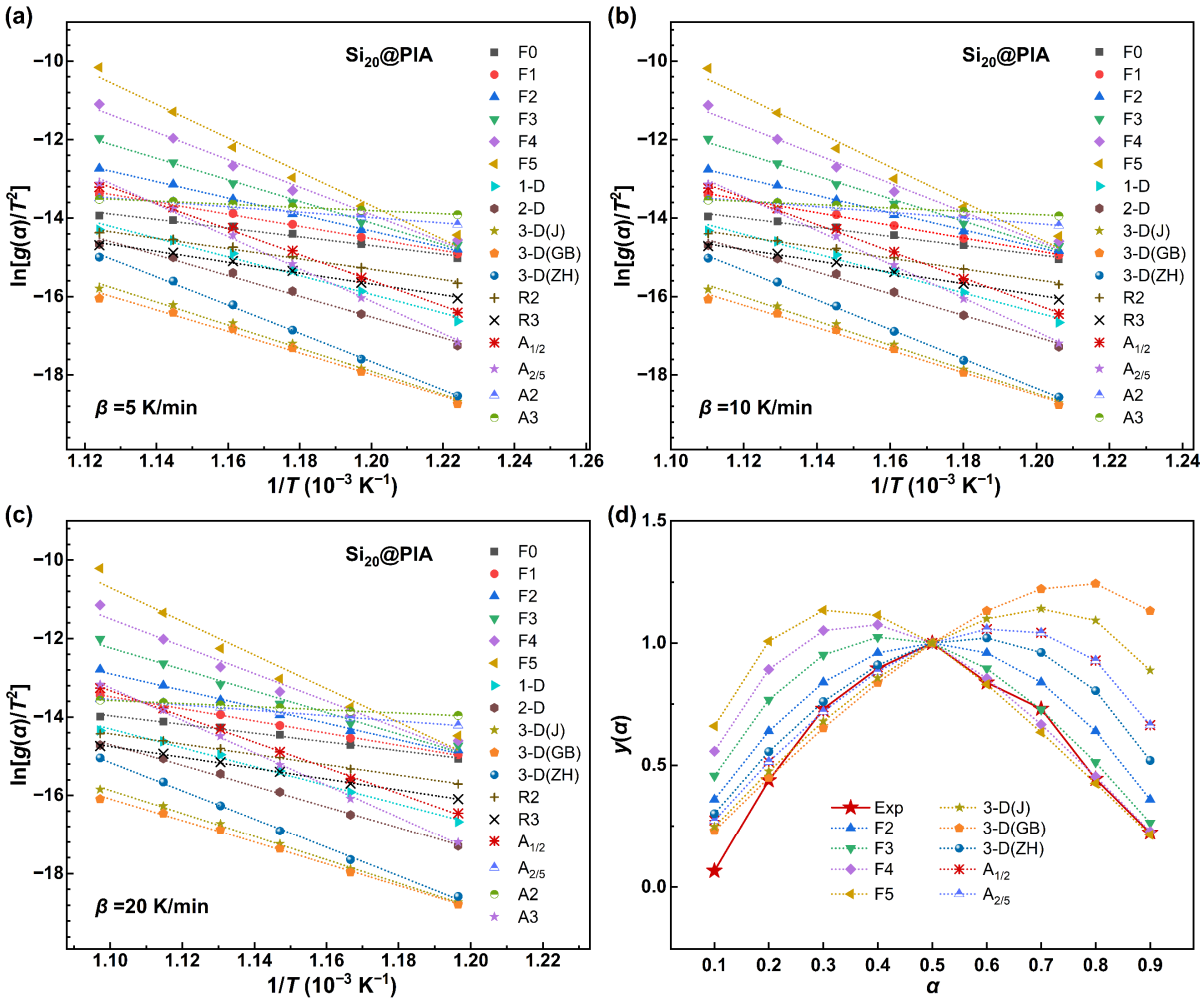

Figure 4. Coats–Redfern (CR) curves (**a**–**c**) with different reaction models of Si@PIAs and correlation of experimental and theoretical curves (**d**) in Si@PIAs pyrolysis determined by the Malek method.

The experimental curves of the pyrolysis process for Si@PIAs were calculated using the Malek method and compared with the theoretical curves of various pyrolysis mechanism function models. The trend of each curve with the conversion rate is shown in Figure 4d. For ease of analysis, the deviation y between each theoretical and the experimental pyrolysis curve was calculated. Meanwhile, comprehensive errors for pyrolysis models were derived by equally weighting y and the CR method calculation error e, with results summarized in Table 4 and Figure S1.

Table 4. Model biases values for different reaction models.

Model	e	y	$\varepsilon = (e + y)/2$
F2	0.526	0.723	0.625
F3	0.379	0.839	0.609
F4	0.211	1.035	0.623
F5	0.029	1.263	0.646
3-D(J)	0.333	0.920	0.627
3-D(GB)	0.379	1.068	0.723
3-D(ZH)	0.185	0.731	0.458
$A_{2/5}$	0.068	0.792	0.430
$A_{1/2}$	0.262	0.792	0.527

Comprehensive errors comparison of various pyrolysis models identified the $A_{2/5}$ random nucleation and growth model ($n = 2/5$) as the most probable mechanism for Si@PIAs pyrolysis. It should be noted, however, that the "nucleation and growth" model is one of the Avrami models within the classification system of solid-state reaction kinetics [44], it is generally interpreted as a phenomenological description that characterizes the random activation of reaction sites and the confined propagation process under structural constraints, and does not imply the definite occurrence of directly observable phase nucleation, interface propagation or morphological growth behaviors in the solid network.

The value of n less than 1 indicates that although thermodynamically feasible, pyrolysis exhibits significant kinetic retardation. This behavior can be attributed to the need to overcome an energy barrier during the initial decomposition stage, with subsequent reaction propagation proceeding slowly under the combined effects of local reactivity, diffusion conditions, and structural constraints. Thus, the presence of the inorganic SiO_2 phase drives a transition in the most probable pyrolysis kinetic model, which shifts from the F3 third-order chemical reaction model of pure PIAs [39] to the $A_{2/5}$ random nucleation and growth model ($n = 2/5$). This shift elevates the difficulty of pyrolysis for Si@PIAs while simultaneously enhancing the thermal safety of the composite aerogels.

The deeper mechanism underlying the transition in pyrolysis behavior can be attributed to the effect of the introduced inorganic SiO_2 phase on the overall structure, heat and mass transfer conditions of polyimide aerogels. On the one hand, the presence of inorganic network alters the spatial distribution of the continuous reaction regions of the organic phase. On the other hand, the nanoporous structure of the Si@PIAs, together with their low thermal conductivity (23 mW/(m·K)), partially intensifies the restricted transfer of heat and volatile decomposition products, thereby further amplifying the kinetic hysteresis effect during pyrolysis. As shown in the simultaneous thermal analysis results, the initial pyrolysis temperature of the Si@PIAs does not significantly increase compared to pure PIAs, but the peak heat flow temperature rises markedly, reflecting the pronounced kinetic retardation of the pyrolysis process.

In contrast, the pyrolysis of pure PIAs can be described by an F3 third-order chemical reaction model, where the reaction rapidly consumes reactants and releases substantial energy once initiated, posing potential thermal hazards. The significantly reduced pyrolysis propensity of the Si@PIAs theoretically confirms that inorganic SiO_2 incorporation substantially improves the thermal safety performance of polyimide aerogels. Furthermore, the GCV of Si@PIAs were measured by oxygen bomb calorimetry (detailed analysis in Figure S2 of the Supplementary Material), confirming that the introduction of inorganic silica dilutes the combustible polyimide component, reducing the heat release of the composites during combustion. This reduction mitigates fire hazard and improves thermal safety, underscoring its practical significance.

3.3. Microstructure

Figure 5 depicts the microstructures of Si@PIA composites with varying inorganic silica loadings (quantified by MTMS volume in the silica sol), revealing distinct microstructural evolutions as the MTMS dosage increases. For Si_5@PIA, the fibrous network of polyimide dominates the microstructure, while the inorganic SiO_2 phase exhibits a sparse distribution. As shown in Figure 5a–c, Si_5@PIA features a uniform, loose, and porous network structure, where the inorganic silica phase is well interwoven with the polyimide aerogel network without causing significant damage to the original structure. At higher magnification, the porous network skeleton displays a regular distribution, with fine granular species sparsely dispersed in some pores. These are inferred to be mildly agglomerated inorganic silicon phases, indicating excellent dispersibility of the inorganic phase in the polyimide matrix at this loading.

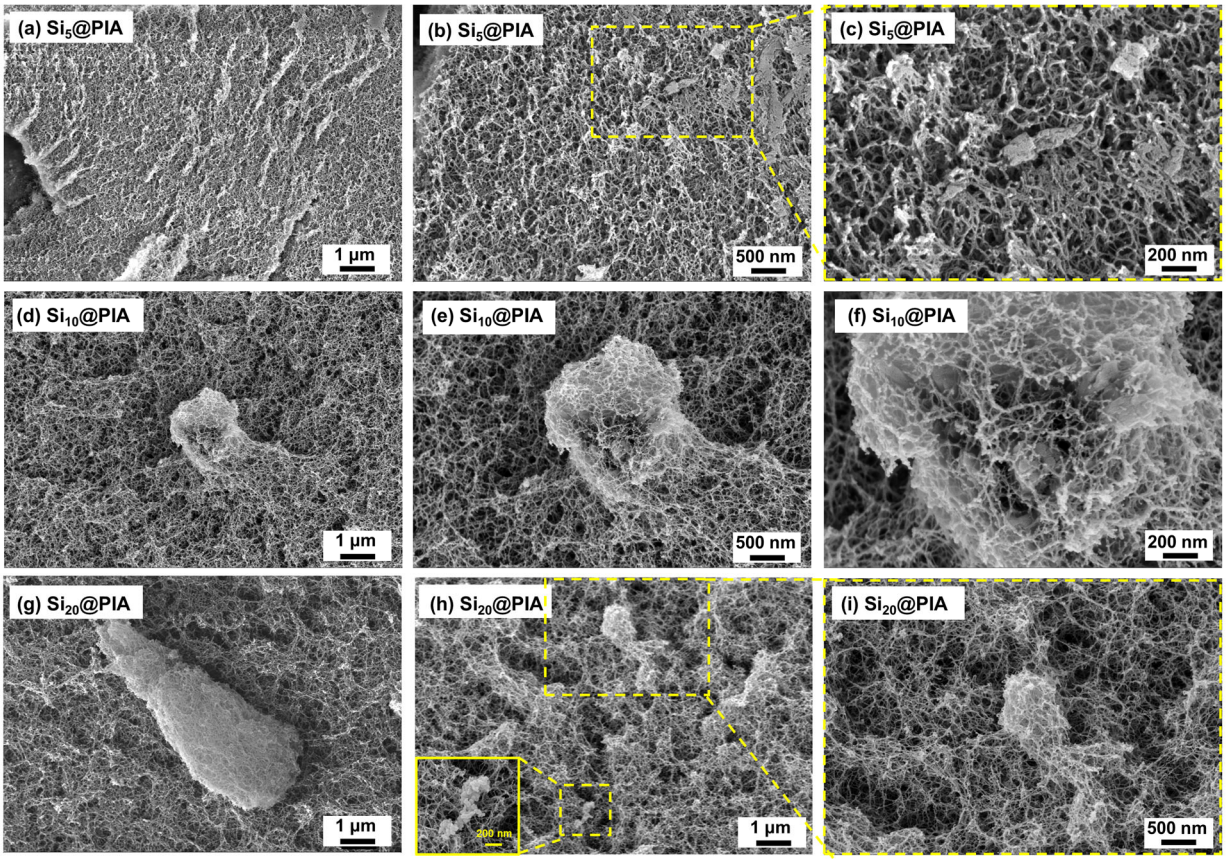

Figure 5. Microstructures of Si@PIA composites. (**a**–**c**) SEM images of Si_5@PIA, where (**b**) and (**c**) are magnified views of (**a**) at different scales. (**d**–**f**) SEM images of Si_{10}@PIA, where (**e**) and (**f**) correspond to magnified views of (**d**) at different scales. (**g**–**i**) SEM images of Si_{20}@PIA, where (**i**) shows a further magnified view of the large dashed-box region in (**h**).

With increasing inorganic SiO_2 loading, SiO_2 remains uniformly dispersed in the polyimide matrix while forming a more complex network structure. As depicted in Figure 5g–h, Si_{20}@PIA presents obvious and large irregular aggregates, significantly exceeding the size of similar structures in Si_5@PIA and Si_{10}@PIA. This may negatively impact the uniformity and connectivity of the polyimide network structure. However, fine network structures persist around the aggregates, indicating that even at high MTMS dosages, the interfacial bonding between the inorganic silica and polyimide organic phase remains stable, enabling effective composite formation.

During co-gel hybridization, moderate MTMS introduction enables sufficient interaction and uniform dispersion between the inorganic silica phase and polyimide molecular chains.

Excessive MTMS, however, causes the inorganic silica phase from hydrolysis and polycondensation to exceed the dispersibility of the polyimide matrix, potentially leading to aggregation. Nevertheless, as shown Figure 5, a relatively uniform and continuous polyimide network is still preserved within and around the aggregated regions, indicating that such local aggregation of the inorganic silica phase does not disrupt the overall continuity of the polyimide network. This behavior can be attributed to the co-gelation synthesis strategy, which enables the inorganic silica skeleton to grow in an interpenetrated and cooperative manner with the polyimide network during gel formation, thereby establishing a more effective structural connectivity. By contrast, in systems prepared via simple physical blending of silica aerogel particles, particle aggregation often significantly weakens the interfacial adhesion between the fillers and the polyimide matrix, resulting in disruption

of the originally uniform and continuous polymer network [20] and potentially leading to pronounced deterioration of material properties. Therefore, compared with physical blending, the co-gelation approach can maintain better structural integrity and stability even when excessive inorganic silica induces local aggregation.

The nitrogen adsorption–desorption isotherms were employed to characterize the pore structure and parameters of Si@PIAs, as presented in Figure 6a. According to the International Union of Pure and Applied Chemistry (IUPAC) classification [45], the curves of Si@PIAs all exhibit typical Type IV isotherms, featuring H3 hysteresis loops in the relative pressure range of $0.6 < P/P_0 < 1.0$. This indicates the presence of abundant mesoporous structures, along with potential slit-shaped interparticle pores (fissure pores) [46]. The disappearance of the saturated adsorption plateau at a relative pressure of approximately 1.0 suggests the existence of macropores and large voids in the Si@PIA composites [47].

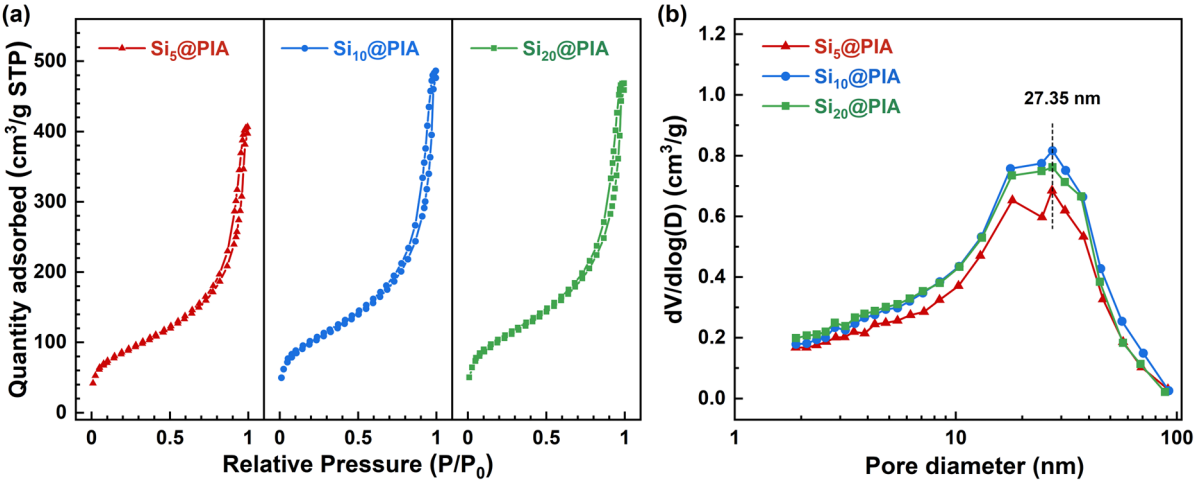

Figure 6. N_2 sorption isotherms (**a**) and pore size distribution (**b**) of Si@PIAs with different content of MTMS.

The pore size distribution curves derived from the BJH method (Figure 6b) show a dominant peak centered at approximately 27.35 nm is observed for all Si@PIA samples. This peak corresponds to the most probable pore diameter, defined as the pore size at which the differential pore volume distribution ($dV/d\log(D)$) reaches its maximum, representing the pore size range that contributes most significantly to the mesopore volume detected by nitrogen adsorption. Compared with pure PIAs [39], which exhibit a most probable pore diameter of approximately 30 nm, the Si@PIA composites show a slight decrease in the most probable pore diameter. This observation indicates that the introduction of the inorganic silica phase does not induce additional fissures or macropores, and that the original network structure of the polyimide aerogel is largely preserved.

The test and calculation data for BET specific surface area, pore volume, and average pore diameter are presented in Table 5. Notably, Si_{10}@PIA and Si_{20}@PIA exhibit larger BET specific surface areas compared to Si_5@PIA, reaching 357.0 m^2/g and 365.7 m^2/g, respectively. This suggests they possess more active adsorption sites, potentially offering better application potential in adsorption, catalysis, and other fields. Minor discrepancies in pore size distribution are observed among samples with varying inorganic silica loadings: the average pore sizes of Si_5@PIA, Si_{10}@PIA, and Si_{20}@PIA are 9.54 nm, 9.86 nm, and 9.24 nm, respectively, all of which are significantly smaller than the corresponding most probable pore diameters. This difference originates from the fact that the average pore diameter and the most probable pore diameter describe different statistical aspects of the pore structure. The average pore diameter represents a geometrically equivalent average

pore diameter under the cylindrical pore assumption, and is influenced by the contribution of smaller mesopores with higher surface area. SEM observations further confirm that the Si@PIA composites possess a pronounced multiscale porous architecture, consisting of a continuous network of fine pores together with larger mesopores and locally loosened macroporous regions. The nitrogen adsorption–desorption and SEM observations probe different pore size regimes and provide complementary information on the multiscale porous structure of the Si@PIAs.

Table 5. Pore parameters of Si@PIAs.

Sample	BET Surface Area (m^2/g)	Pore Volume [a] (cm^3/g)	Average pore Diameter [b] (nm)
Si_5@PIA	306.0 ± 1.3	0.60	9.54
Si_{10}@PIA	357.0 ± 1.7	0.71	9.86
Si_{20}@PIA	365.7 ± 1.6	0.68	9.24

[a,b] The pore volume and average pore diameter were derived from nitrogen desorption. Uncertainties: The BET surface area is approximately 50 m^2/g; pore volume and average pore diameter have a relative uncertainty of 5% [21].

3.4. Basic Physicochemical Characteristics

3.4.1. Density, Shrinkage and Thermal Conductivity

As shown in Figure 7a, the density of Si@PIAs decreases initially and then stabilizes with increasing inorganic silica loading. When the MTMS volume in silica sol is 5 mL, the Si_5@PIA exhibits a relatively high density of 108 mg/cm^3. As the MTMS volume increases to 10 mL, the density significantly drops to 85 mg/cm^3. Further increases in MTMS volume to 15 mL and 20 mL result in a gentle change in density. The incorporation of MTMS forms SiO_2 aerogels, which fills part of the voids within the polyimide fiber network and compacts the overall structure. Given that SiO_2 aerogel itself has a low density, the density of Si@PIAs decreases accordingly. In terms of shrinkage rate, as the MTMS content in silica sol increases from 5 mL to 20 mL, the shrinkage rate of Si@PIAs decreases monotonically, reducing from 10.3% (for pure polyimide aerogel) to 3.3%. The inorganic silica phase effectively enhances the stability of the aerogel skeleton, mitigating volume shrinkage of polyimide during the gelation and supercritical drying processes.

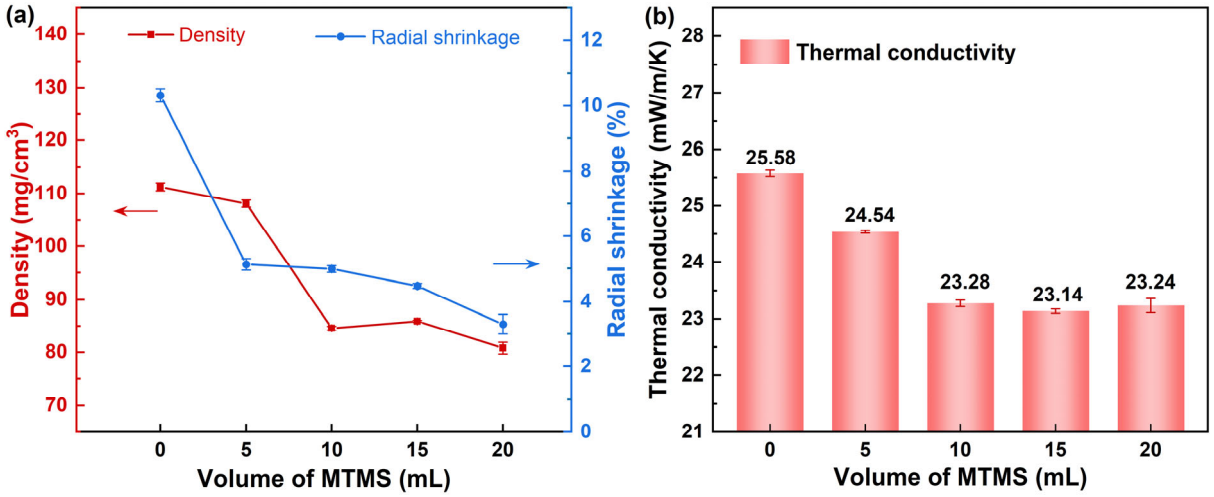

Figure 7. Density and radial shrinkage (**a**), thermal conductivity (**b**) of Si@PIAs with different content of MTMS.

Figure 7b shows that the thermal conductivity of Si@PIAs exhibits a variation trend similar to that of their density. Within the range of V_{MTMS} < 10 mL, the thermal conduc-

tivity gradually decreases with increasing inorganic SiO_2 content. This phenomenon is attributed to the nanoporous structure of SiO_2 aerogel, which effectively suppresses heat conduction and enhances thermal resistance. When the introduction amount exceeds a certain threshold, agglomeration may occur due to the non-uniform dispersion of silica sol. Moreover, excessive silica sol can interfere with the network cross-linking and gelation process of polyimide, ultimately disrupting the original uniform fibrous nanoporous structure and leading to a slight increase in thermal conductivity. Notably, Si@PIAs still show significantly lower thermal conductivity than pure polyimide aerogel, indicating that the inorganic SiO_2 can effectively reduce the thermal conductivity of PIAs.

3.4.2. Surface Chemistry

To characterize the surface chemical functional groups of Si@PIA composites upon inorganic SiO_2 incorporation, Figure 8 displays the FTIR spectra. For all Si@PIAs, no formation of new chemical bonds is observed, but distinct absorption bands of Si-O-Si bonds emerge at approximately 1080 cm^{-1}. This result provides qualitative evidence that the inorganic silica phase has been successfully introduced into the Si@PIA composite aerogels with the concomitant formation of a silica-oxygen network structure.

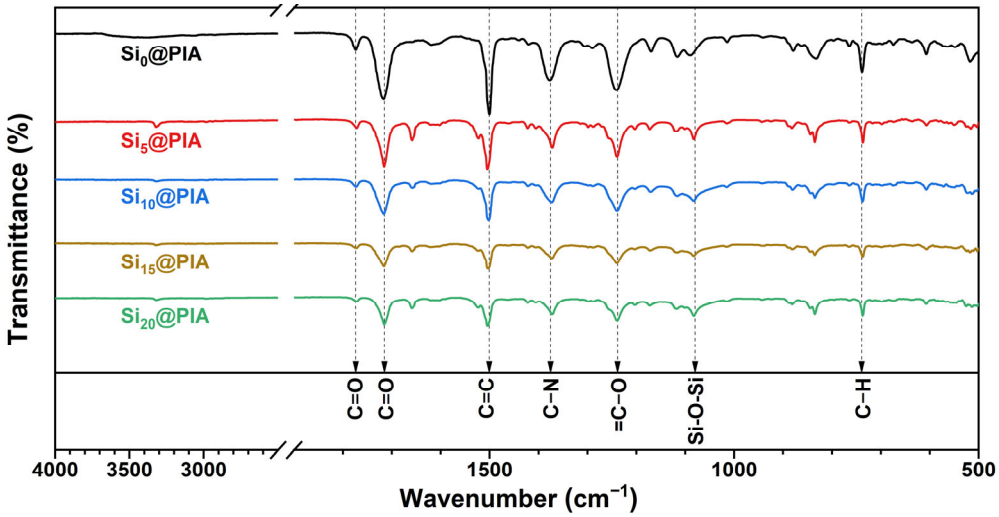

Figure 8. FTIR spectra of Si@PIAs with different content of MTMS.

Meanwhile, the characteristic imide ring peaks at 1376 cm^{-1} (C-N stretching), 1716 cm^{-1}, and 1775 cm^{-1} (asymmetric/symmetric C=O stretching) remain prominent [8,48]. The absorption peaks at 1501 cm^{-1} and 739 cm^{-1} are assigned to the stretching vibration of C=C bonds and the bending vibration of C-H bonds in benzene rings, respectively. The persistence of these polyimide characteristic absorption peaks demonstrates that the fundamental structure of polyimide remains intact during the hybridization process, confirming effective hybridization between the two components. Since no chemical bond cross-linking between the inorganic silicon phase and the polyimide matrix was detected in the FTIR results, further discussion on the chemical bonding status of Si@PIAs via XPS or solid-state NMR measurements is no longer provided.

3.5. Performance Comparison

3.5.1. Comparison with Pure PIAs

The performance comparison between Si_{10}@PIA and PIA is presented in Figure 9c. The in situ incorporation of the inorganic silicon phase effectively enhances the comprehensive properties of the material, thereby achieving a true synergistic integration of the

organic polyimide phase and the inorganic silicon phase. Compared with PIA, Si_{10}@PIA exhibits enhanced thermal insulation performance, with a thermal conductivity lower than that of air. In terms of dimensional stability, Si_{10}@PIA also shows improvement, as the shrinkage rate of the sample during fabrication is reduced to below 5%. Furthermore, the in situ incorporation of the inorganic silicon phase effectively increases the T_{onset} and the average reaction activation energy during pyrolysis. This elevates the difficulty of thermal decomposition for Si_{10}@PIA and retards the pyrolysis process, allowing Si_{10}@PIA to maintain its own stability for a longer period under the same conditions. Meanwhile, the reduction in the GCV of Si_{10}@PIA indicates a decrease in the heat released during its combustion process, thereby contributing to a lower fire hazard.

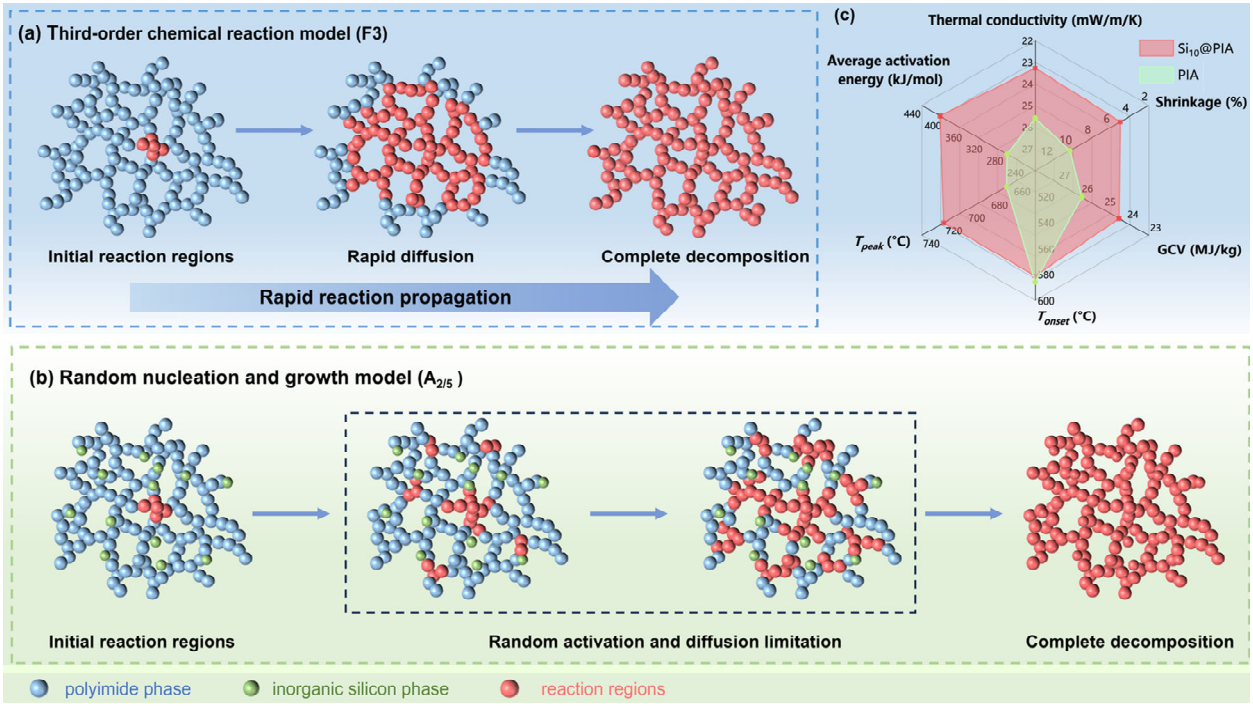

Figure 9. Idealized schematic illustrations of the kinetic models used to describe the pyrolysis behavior of PIA (**a**) and Si@PIAs (**b**), Schematic representations are intended to illustrate kinetic behaviors only and do not represent actual microstructural evolution. Comparison of multiple properties (**c**) between PIA [39] and Si_{10}@PIA.

In addition, a transition in the kinetic description of the pyrolysis process is observed. The pyrolysis behavior of pure PIAs can be well described by an F3 third-order chemical reaction model, whose idealized schematic representation is shown in Figure 9a. This model reflects a reaction regime in which reactants are rapidly consumed and a large amount of energy is released once the pyrolysis reaction initiates. In contrast, the pyrolysis mechanism of Si@PIAs is better described by an $A_{2/5}$ random nucleation and growth model ($n = 2/5$), as illustrated by the corresponding idealized kinetic schematic in Figure 9b. This transition further confirms theoretically that the introduction of inorganic SiO_2 enables a significant improvement in the thermal safety performance of polyimide aerogels, which holds important practical significance.

3.5.2. Comparison with Previous Studies

To better evaluate the advantages and positioning of the present work, a comparison of key performance parameters and research scope between this study and previously reported SiO_2 aerogel/polyimide aerogel composites is summarized in Table 6. It can

be seen that the Si@PIA composites achieve higher onset decomposition temperatures than those reported in the literature, while simultaneously maintaining low density, low shrinkage, and low thermal conductivity. Moreover, previous studies have rarely focused on the peak decomposition temperature of the composites. In contrast, through the in situ co-gelation introduction of the inorganic silica phase, the peak decomposition temperature in this work is increased to as high as 720.7 °C, indicating a markedly enhanced resistance to thermal decomposition.

Table 6. Comparison of performance with previously reported studies.

Sample	Synthesis Strategy	Density (mg/cm^3)	Thermal Conductivity mW/(m·K)	Shrinkage (%)	T_{onset} or $T_{5\%}$ (°C)	Refs.
PIA-100 wt%	Particle doping	160.0	36.0	20.0	535.0	[19]
PI-20	Particle doping	85.0	20.1	9.2	559.7	[20]
PI/SiO_2-2	Particle doping	70.0	21.8	<20	Unreported	[49]
SiO_2/PI-10	Co-gelation	60.7	37.4	Unreported	542.0	[24]
SiO_2/PI-3	Co-gelation	Unreported	31.1	Unreported	542.0	[50]
PI-5 wt%	Co-gelation	132.0	30.6	15.8	360.0	[51]
PISA-1	Co-gelation	32.8	37.9	19.7	532.0	[52]
Si_{10}@PIA	Co-gelation	84.6	23.3	5.0	581.3	This work

From a research scope perspective, this study provides a detailed pyrolysis kinetic analysis of the Si@PIA composites, aiming to describe their thermal decomposition behavior and underlying mechanisms from a kinetic standpoint and to clarify the beneficial role of the inorganic silica phase in improving thermal stability. Such systematic kinetic investigations have been scarcely addressed in prior studies on SiO_2 aerogel/polyimide aerogel composites, and this aspect constitutes the primary innovation and scientific significance of the present work.

4. Conclusions

This study optimizes the dimensional stability, thermal insulation performance and thermal safety of PIAs, by fabricating Si@PIA composites via organic–inorganic co-gelation using MTMS as the silicon source. With increasing inorganic silica content, the shrinkage rate of Si@PIAs during preparation gradually decreased, significantly improving dimensional stability. Thermal conductivity first decreased and then slightly increased but remained significantly lower than that of pure PIAs. Among them, Si_{10}@PIA exhibited optimal comprehensive performance, with a density of 85 mg/cm^3, a thermal conductivity of 23.28 mW/(m·K), and a peak thermal stability temperature of 720.7 °C. The inorganic silica phase successfully integrated into the PIA system to form a Si-O-Si network structure without damaging the fundamental polyimide framework. In terms of thermal safety performance, the inorganic SiO_2 network hindered polyimide thermal decomposition, improved thermal stability, and reduced GCV. Additionally, it retarded the pyrolysis of PIAs, enhancing high-temperature stability. Pyrolysis kinetics analysis revealed that Si@PIAs were more difficult to pyrolyze than pure PIAs. Model-fitting methods identified the most probable pyrolysis mechanism as a random nucleation and growth model (n = 2/5, $g(\alpha) = [-\ln(1-\alpha)]^{5/2}$), indicating significant kinetic retardation and low pyrolysis propensity. These findings provide critical experimental and theoretical insights for optimizing the performance of Si@PIAs, facilitating their application in high-performance thermal insulation materials, thermal protection systems, and other advanced technological fields.

Supplementary Materials: The following supporting information can be downloaded at: https://www.mdpi.com/article/10.3390/fire9020081/s1, Table S1: Thermal dynamic parameters of Si@PIAs in the pyrolysis process. Figure S1: Model biases of different reaction models. Figure S2: GCV of Si@PIAs.

Author Contributions: Z.L.: Writing—review and editing, Supervision, Funding acquisition, Conceptualization. F.Z.: Writing—original draft, Visualization, Investigation, Formal analysis. K.S.: Investigation, Validation. M.L.: Writing—review & editing, Visualization. Y.D.: Visualization, Investigation. J.C.: Investigation, Conceptualization. S.L.: Writing—review & editing, Visualization. H.Y.: Visualization, Investigation. All authors have read and agreed to the published version of the manuscript.

Funding: This work is supported by the National Natural Science Foundation of China (No. 52274248), the Natural Science Foundation of Hunan Province (No. 2025JJ40051), the Opening Fund of Key Laboratory of Civil Aviation Thermal Hazards Prevention and Emergency Response, Civil Aviation University of China (No. RZH2022-KF-03), the Postgraduate Scientific Research Innovation Project of Hunan Province (No. CX20250329) and the Fundamental Research Funds for the Central Universities of Central South University (No. 2025ZZTS0274). Major National Science and Technology Project for Deep Earth of China: 2024ZD1003808.

Data Availability Statement: The raw data supporting the conclusions of this article will be made available by the authors on request.

Acknowledgments: This work was also supported in part by the High Performance Computing Center of Central South University. The authors extend their gratitude to Yang Ting from Scientific Compass (www.shiyanjia.com) for providing invaluable assistance with the SEM analysis.

Conflicts of Interest: The authors declare no conflict of interest.

References

1. Sun, Y.; Wang, Z.; Zhao, J.; Nie, H.; Zhou, G. Low shrinkage polyimide aerogels with excellent thermal insulation: Boosted by "paddle-shaped" benzhydrylidenefluorene-based diamines. *Chem. Eng. J.* **2024**, *479*, 147642. [CrossRef]
2. Ghaffari-Mosanenzadeh, S.; Tafreshi, O.A.; Karamikamkar, S.; Saadatnia, Z.; Rad, E.; Meysami, M.; Naguib, H.E. Recent advances in tailoring and improving the properties of polyimide aerogels and their application. *Adv. Colloid Interface Sci.* **2022**, *304*, 102646. [CrossRef] [PubMed]
3. Guo, H.; Meador, M.A.B.; McCorkle, L.; Quade, D.J.; Guo, J.; Hamilton, B.; Cakmak, M.; Sprowl, G. Polyimide Aerogels Cross-Linked through Amine Functionalized Polyoligomeric Silsesquioxane. *ACS Appl. Mater. Interfaces* **2011**, *3*, 546–552. [CrossRef] [PubMed]
4. Feng, J.; Wang, X.; Jiang, Y.; Du, D.; Feng, J. Study on Thermal Conductivities of Aromatic Polyimide Aerogels. *ACS Appl. Mater. Interfaces* **2016**, *8*, 12992–12996. [CrossRef]
5. Xi, S.; Wang, Y.; Zhang, X.; Cao, K.; Su, J.; Shen, J.; Wang, X. Fire-resistant polyimide-silica aerogel composite aerogels with low shrinkage, low density and high hydrophobicity for aerospace applications. *Polym. Test.* **2023**, *129*, 108259. [CrossRef]
6. Wang, J.; Yue, X.; Li, X.; Dong, J.; Zhang, Q.; Zhao, X. Lightweight and Elastic Silver Nanowire/PEDOT:PSS/Polyimide Aerogels for Piezoresistive Sensors. *ACS Appl. Polym. Mater.* **2022**, *4*, 3205–3216. [CrossRef]
7. Chen, Y.; Shao, G.; Kong, Y.; Shen, X.; Cui, S. Facile preparation of cross-linked polyimide aerogels with carboxylic functionalization for CO_2 capture. *Chem. Eng. J.* **2017**, *322*, 1–9. [CrossRef]
8. Deng, Y.; Pan, Y.; Zhang, Z.; Fu, Y.; Gong, L.; Liu, C.; Yang, J.; Zhang, H.; Cheng, X. Novel Thermotolerant and Flexible Polyimide Aerogel Separator Achieving Advanced Lithium-Ion Batteries. *Adv. Funct. Mater.* **2022**, *32*, 2106176. [CrossRef]
9. Wu, S.; Du, A.; Huang, S.; Sun, W.; Xiang, Y.; Zhou, B. Solution-processable polyimide aerogels with high hydrophobicity. *Mater. Lett.* **2016**, *176*, 118–121. [CrossRef]
10. Liu, C.; Wang, M.; Wang, J.; Xu, G.; Zhang, S.; Ding, F. Double-Phase-Networking Polyimide Hybrid Aerogel with Exceptional Dimensional Stability for Superior Thermal Protection System. *Small* **2024**, *20*, 2404104. [CrossRef]
11. Smirnova, I.; Gurikov, P. Aerogel production: Current status, research directions, and future opportunities. *J. Supercrit. Fluids* **2018**, *134*, 228–233. [CrossRef]
12. Mahadik, S.; Pedraza, F.; Parale, V.; Park, H.-H. Organically modified silica aerogel with different functional silylating agents and effect on their physico-chemical properties. *J. Non-Cryst. Solids* **2016**, *453*, 164–171. [CrossRef]
13. He, J.; Zhao, H.; Li, X.; Su, D.; Zhang, F.; Ji, H.; Liu, R. Superelastic and superhydrophobic bacterial cellulose/silica aerogels with hierarchical cellular structure for oil absorption and recovery. *J. Hazard. Mater.* **2018**, *346*, 199–207. [CrossRef] [PubMed]

14. Lei, Y.; Chen, X.; Song, H.; Hu, Z.; Cao, B. The influence of thermal treatment on the microstructure and thermal insulation performance of silica aerogels. *J. Non-Cryst. Solids* **2017**, *470*, 178–183. [CrossRef]
15. Randall, J.P.; Meador, M.A.B.; Jana, S.C. Tailoring Mechanical Properties of Aerogels for Aerospace Applications. *ACS Appl. Mater. Interfaces* **2011**, *3*, 613–626. [CrossRef]
16. Feng, J.; Le, D.; Nguyen, S.T.; Nien, V.T.C.; Jewell, D.; Duong, H.M. Silica-cellulose hybrid aerogels for thermal and acoustic insulation applications. *Colloids Surf. A Physicochem. Eng. Asp.* **2016**, *506*, 298–305. [CrossRef]
17. Zhou, F.; Gu, H.-Z.; Wang, C.-F. Preparation and microstructure of in-situ gel modified expanded vermiculite. *Ceram. Int.* **2013**, *39*, 4075–4079. [CrossRef]
18. Tang, X.; Sun, A.; Chu, C.; Yu, M.; Ma, S.; Cheng, Y.; Guo, J.; Xu, G. A novel silica nanowire-silica composite aerogels dried at ambient pressure. *Mater. Des.* **2017**, *115*, 415–421. [CrossRef]
19. Ma, B.; Hou, X.; Li, Y. Mechanically strong and thermal insulating polyimide/SiO_2 aerogel prepared by ambient drying. *Mater. Lett.* **2022**, *327*, 133039. [CrossRef]
20. Zhang, T.; Zhao, Y.; Li, X.; Ma, X.; Li, S.; Sun, M.; Liu, H.; Wang, K. Ultralight and heat-insulating mesoporous polyimide aerogels cross-linked with aminated SiO_2 nanoparticles. *Microporous Mesoporous Mater.* **2021**, *319*, 111074. [CrossRef]
21. Kantor, Z.; Wu, T.; Zeng, Z.; Gaan, S.; Lehner, S.; Jovic, M.; Bonnin, A.; Pan, Z.; Mazrouei-Sebdani, Z.; Opris, D.M.; et al. Heterogeneous silica-polyimide aerogel-in-aerogel nanocomposites. *Chem. Eng. J.* **2022**, *443*, 136401. [CrossRef]
22. Rhine, W.; Wang, J.; Begag, R. Polyimide Aerogels, Carbon Aerogels, and Metal Carbide Aerogels and Methods of Making Same. Patent US7074880B2, 11 July 2006.
23. Leventis, N.; Chandrasekaran, N.; Sadekar, A.G.; Mulik, S.; Sotiriou-Leventis, C. The effect of compactness on the carbothermal conversion of interpenetrating metal oxide/resorcinol-formaldehyde nanoparticle networks to porous metals and carbides. *J. Mater. Chem.* **2010**, *20*, 7456–7471. [CrossRef]
24. Xiao, Z.; Che, J.; Li, H.; Yue, X.; Yu, X.; Sun, F.; Xue, C.; Xiang, J. Superhydrophobic and elastic silica/polyimide aerogel based on double confinement growth strategy of the co-sol system. *Mater. Chem. Front.* **2022**, *6*, 482–490. [CrossRef]
25. Yan, P.; Zhou, B.; Du, A. Synthesis of polyimide cross-linked silica aerogels with good acoustic performance. *RSC Adv.* **2014**, *4*, 58252–58259. [CrossRef]
26. Zhu, M.; Li, W.; Yang, S.; Zou, P.; Zhang, Y.; Xu, M.; Li, S.; Tang, X.; Lu, Y.; Lai, K.; et al. Ambient pressure dried polyimide/silica aerogels for efficient radar stealth at high temperature. *Compos. Commun.* **2025**, *56*, 102338. [CrossRef]
27. Sing, K. The use of nitrogen adsorption for the characterisation of porous materials. *Colloids Surf. A Physicochem. Eng. Asp.* **2001**, *187–188*, 3–9. [CrossRef]
28. Reichenauer, G. Structural Characterization of Aerogels. In *Aerogels Handbook*; Aegerter, M.A., Leventis, N., Koebel, M.M., Eds.; Springer: New York, NY, USA, 2011; pp. 449–498.
29. He, S.; Li, Z.; Ma, Y.; Liu, X.; Jin, X.; He, C.; Du, C.; Li, P.; Huang, D. Thermal decomposition of hydrophobic silica aerogels: Kinetics and reaction mechanism. *J. Therm. Anal. Calorim.* **2023**, *148*, 13941–13957. [CrossRef]
30. Vyazovkin, S. Computational aspects of kinetic analysis.: Part C. The ICTAC Kinetics Project—The light at the end of the tunnel? *Thermochim. Acta* **2000**, *355*, 155–163. [CrossRef]
31. Özsin, G. Exploring the Thermal Degradation of Bakelite: Non-Isothermal Kinetic Modeling, Thermodynamic Insights, and Evolved Gas Analysis via Integrated In Situ TGA/MS and TGA/FT-IR Techniques. *Polymers* **2025**, *17*, 2197. [CrossRef]
32. Starink, M.J. The determination of activation energy from linear heating rate experiments: A comparison of the accuracy of isoconversion methods. *Thermochim. Acta* **2003**, *404*, 163–176. [CrossRef]
33. Flynn, J.H.; Wall, L.A. A quick, direct method for the determination of activation energy from thermogravimetric data. *J. Polym. Sci. Part B Polym. Lett.* **1966**, *4*, 323–328. [CrossRef]
34. Ozawa, T. A new method of analyzing thermogravimetric data. *Bull. Chem. Soc. Jpn.* **1965**, *38*, 1881–1886. [CrossRef]
35. Ahmad, M.S.; Mehmood, M.A.; Taqvi, S.T.H.; Elkamel, A.; Liu, C.-G.; Xu, J.; Rahimuddin, S.A.; Gull, M. Pyrolysis, kinetics analysis, thermodynamics parameters and reaction mechanism of *Typha latifolia* to evaluate its bioenergy potential. *Bioresour. Technol.* **2017**, *245*, 491–501. [CrossRef] [PubMed]
36. Liu, Q.; Wang, Z.; Xie, L.; Chen, Z.; Wu, X.; Li, Z. A polyimide separator inlaid by methylsilyl-modified silica aerogels for high thermal safety and low polarization lithium-ion battery. *J. Power Sources* **2024**, *607*, 234585. [CrossRef]
37. Coats, A.W.; Redfern, J.P. Kinetic Parameters from Thermogravimetric Data. *Nature* **1964**, *201*, 68–69. [CrossRef]
38. Yao, C.; Wang, X.; Zhou, Y.; Jin, X.; Song, L.; Hu, Y.; Zeng, W. Thermogravimetric analysis and kinetics characteristics of typical grains. *J. Therm. Anal. Calorim.* **2021**, *143*, 647–659. [CrossRef]
39. Li, Z.; Shen, K.; Hu, M.; Liu, M.; Zhou, F.; Li, M.; Liu, Q.; Wu, X.; Chen, W. Pyrolysis behavior, kinetics, and mechanism of polyimide aerogels. *J. Anal. Appl. Pyrolysis* **2025**, *189*, 107108. [CrossRef]
40. Li, Z.; Zhou, F.; Shen, K.; Hu, M.; Liu, M.; Yao, S.; Chen, Z.; Liu, Q.; Fan, C.; Wu, X. Tuning macroporous structure and thermal properties of polymethylsilsesquioxane aerogels via tailored heat treatment. *J. Non-Cryst. Solids* **2025**, *651*, 123388. [CrossRef]

41. Vyazovkin, S.; Burnham, A.K.; Criado, J.M.; Pérez-Maqueda, L.A.; Popescu, C.; Sbirrazzuoli, N. ICTAC Kinetics Committee recommendations for performing kinetic computations on thermal analysis data. *Thermochim. Acta* **2011**, *520*, 1–19. [CrossRef]
42. Lyon, R.E.; Safronava, N.; Senese, J.; Stoliarov, S.I. Thermokinetic model of sample response in nonisothermal analysis. *Thermochim. Acta* **2012**, *545*, 82–89. [CrossRef]
43. Burnham, A.K.; Braun, R.L. Global Kinetic Analysis of Complex Materials. *Energy Fuels* **1999**, *13*, 1–22. [CrossRef]
44. Khawam, A.; Flanagan, D.R. Solid-State Kinetic Models: Basics and Mathematical Fundamentals. *J. Phys. Chem. B* **2006**, *110*, 17315–17328. [CrossRef] [PubMed]
45. Rojas, F.; Kornhauser, I.; Felipe, C.; Esparza, J.M.; Cordero, S.; Domínguez, A.; Riccardo, J.L. Capillary condensation in heterogeneous mesoporous networks consisting of variable connectivity and pore-size correlation. *Phys. Chem. Chem. Phys.* **2002**, *4*, 2346–2355. [CrossRef]
46. Sing, K.S.W.; Williams, R.T. Physisorption Hysteresis Loops and the Characterization of Nanoporous Materials. *Adsorpt. Sci. Technol.* **2004**, *22*, 773–782. [CrossRef]
47. Sun, Z.; Zhao, Z.; Kong, Y.; Ren, J.; Jiang, X.; Shen, X. Auto-Continuous Synthesis of Robust and Hydrophobic Silica Aerogel Microspheres from Low-Cost Aqueous Sodium Silicate for Fast Dynamic Organics Removal. *Gels* **2022**, *8*, 778. [CrossRef]
48. Nguyen, B.N.; Meador, M.A.B.; Scheiman, D.; McCorkle, L. Polyimide Aerogels Using Triisocyanate as Cross-linker. *ACS Appl. Mater. Interfaces* **2017**, *9*, 27313–27321. [CrossRef]
49. Fan, W.; Zhang, X.; Zhang, Y.; Zhang, Y.; Liu, T. Lightweight, strong, and super-thermal insulating polyimide composite aerogels under high temperature. *Compos. Sci. Technol.* **2019**, *173*, 47–52. [CrossRef]
50. Zhang, X.; Ni, X.; Li, C.; You, B.; Sun, G. Co-gel strategy for preparing hierarchically porous silica/polyimide nanocomposite aerogel with thermal insulation and flame retardancy. *J. Mater. Chem. A* **2020**, *8*, 9701–9712. [CrossRef]
51. Fei, Z.; Yang, Z.; Chen, G.; Li, K. Preparation of tetraethoxysilane-based silica aerogels with polyimide cross-linking from 3, 3′, 4, 4′-biphenyltetracarboxylic dianhydride and 4, 4′-oxydianiline. *J. Sol-Gel Sci. Technol.* **2018**, *85*, 506–513. [CrossRef]
52. Wang, S.; Wang, H.; Wang, W.; Li, H.; Yang, J.; Li, D. Fabrication of PI/SiO_2 composite aerogels via an in-situ co-gel strategy for integrated thermal and acoustic insulation. *J. Mater. Sci. Technol.* **2026**, *245*, 208–220. [CrossRef]

Disclaimer/Publisher's Note: The statements, opinions and data contained in all publications are solely those of the individual author(s) and contributor(s) and not of MDPI and/or the editor(s). MDPI and/or the editor(s) disclaim responsibility for any injury to people or property resulting from any ideas, methods, instructions or products referred to in the content.